



**HAL**  
open science

## Robust identification of elasto-plastic constitutive law parameters from digital images using 3D kinematics

Julien Réthoré, . Muhibullah, Thomas Elguedj, Michel Coret, Philippe Chaudet, Alain Combescure

### ► To cite this version:

Julien Réthoré, . Muhibullah, Thomas Elguedj, Michel Coret, Philippe Chaudet, et al.. Robust identification of elasto-plastic constitutive law parameters from digital images using 3D kinematics. International Journal of Solids and Structures, 2013, 50 (1), pp.73-85. 10.1016/j.ijsolstr.2012.09.002 . hal-01007267

**HAL Id: hal-01007267**

**<https://hal.science/hal-01007267>**

Submitted on 3 Jun 2017

**HAL** is a multi-disciplinary open access archive for the deposit and dissemination of scientific research documents, whether they are published or not. The documents may come from teaching and research institutions in France or abroad, or from public or private research centers.

L'archive ouverte pluridisciplinaire **HAL**, est destinée au dépôt et à la diffusion de documents scientifiques de niveau recherche, publiés ou non, émanant des établissements d'enseignement et de recherche français ou étrangers, des laboratoires publics ou privés.



Distributed under a Creative Commons Attribution 4.0 International License

# Robust identification of elasto-plastic constitutive law parameters from digital images using 3D kinematics

Julien Réthoré, Muhibullah, Thomas Elguedj, Michel Coret, Philippe Chaudet, Alain Combescure

Université de Lyon, CNRS, INSA-Lyon, Laboratoire de Mécanique des Contacts et des Structures, UMR5259, F-69621 Villeurbanne, France

Identification and model validation have been performed for decades using global response of samples or structures. Nowadays, the development of full field measurement techniques offers the opportunity to take benefit of a much larger amount of experimental data. Existing strategies that can handle full field data to estimate constitutive model parameters are limited to two-dimensional mechanical models. In some cases, such as finite strain plasticity, two-dimensional modeling is not acceptable and three-dimensional effects must be accounted for. In this paper, we propose an identification strategy that mixes intimately numerical simulations with digital image correlation and that can overcome the common limitations of existing methods. It is shown to be noise robust, to have a low sensitivity to initial parameter guess and to mesh refinement. Furthermore, the proposed strategy allows to discriminate between constitutive models that give similar global responses.

**Keywords:**  
Identification  
Full field measurement  
Digital image correlation  
Non-linear constitutive law  
Finite element

## 1. Introduction

Before any practical use, a constitutive model must be identified and validated. Uniaxial and homogeneous strain states were first used in experiments in order to be able to convert directly strains into stresses so that constitutive parameters are evaluated directly from global measurements of a resultant force. However, for cases such as plasticity, it is well known that triaxiality plays an important role and that its effect must be accounted for in the constitutive model. In such a case, the direct procedure that was used for uniaxial tests becomes useless. To circumvent this limitation, coupling numerical simulation with experiments is unavoidable. Based on global measurements, the Finite Element Model Updating technique was proposed by Kavanagh and Clough (1971). For the past twenty years, full field measurement techniques have been extensively developed in the experimental mechanics community. Among those techniques, the most popular is Digital Image Correlation (DIC) (see *e.g.*, Besnard et al., 2006; Sun et al., 2005; Sutton et al., 1983). Full field measurement techniques offer the possibility to acquire a large amount of experimental data that might be useful in the context of identification of constitutive law parameters.

Various identification techniques coupled with full field measurements are now available, amongst which are the Virtual Field Method (Grédiac, 1989), the Equilibrium Gap Method (Claire et al., 2004), the Constitutive Equation Gap Method (Pagnacco

et al., 2007), the Reciprocity Gap Method (Bui et al., 2004), and Finite Element Model Updating (Lecompte et al., 2007). Avril et al. (2008) and Grédiac et al. (2006) give an overview of these methods. To the authors' knowledge, these methods have a common limitation: they are restricted to two-dimensional applications when 2D full field data are analyzed. However, in some case, *e.g.*, for thick specimens made of an elasto-plastic material, three-dimensional effects should not be neglected. The use of stereo-correlation systems on both side of a specimen were used in Wu et al. (2011) in order to extract out of plane averaged through the thickness strain components. Contrary to the previously mentioned techniques, the framework proposed in Réthoré (2010) can be extended to three-dimensional kinematics. Note that the Virtual Field Method has been extended to the use of 3D data recently in Rossi and Pierron (2011). In this paper, we propose to couple strongly DIC with numerical simulation in a single analysis that also allows to estimate the parameters of the constitutive law in the numerical model. Unlike DIC that concerns only the samples' surface, we develop in this paper a method in which the mechanical model can have 3D kinematics. Furthermore, the original approach introduced in Réthoré (2010) requires some adaptations in order to be able to deal with elastic plastic constitutive laws efficiently. This will be detailed throughout the paper, where the approach is also extended to multiple camera systems.

First, notations and the general framework of the method are described in Section 2. After recalling briefly the original approach proposed in Réthoré (2010), Section 2 presents its extension to a larger class of constitutive laws. Section 3 is devoted to the generalization of the proposed framework to the use of 3D kinematics

and multiple camera systems. Then, a virtual testing procedure is elaborated in order to evaluate the performance of the approach in Section 4. In closing, a real experiment is analyzed in Section 5.

## 2. Integrated mechanical image correlation (I-MIC)

### 2.1. General settings and notations

In the following, we adopt a Finite Element discretization for the displacement field. The discretized displacement field reads:

$$\mathbf{u}(\mathbf{x}) = \sum_{k \in \mathcal{N}} u_k \mathbf{N}_k(\mathbf{x}) = [\mathbf{N}]\{\mathbf{U}\}, \quad (1)$$

where  $\mathcal{N}$  is the set of finite element degrees of freedom (DOFs), and  $\mathbf{N}_k$  the finite element shape functions associated with a predefined finite element mesh. A matrix form of this equation is also used:  $[\mathbf{N}]$  is a matrix that collects the value of the  $\mathcal{N}$  vector shape functions at a given location  $\mathbf{x}$  and  $\{\mathbf{U}\}$  the vector that collects the values of the displacement Degrees Of Freedom (DOF). Note that  $[\mathbf{N}]$  has  $\mathcal{N}$  columns and as many lines as points where the shape functions are evaluated. For clarity, the positions of these evaluation points are omitted by the notation. A matrix–vector format is also adopted for the images data. For an image  $f$ ,  $\mathbf{F}$  is a column vector that contains the grey level of each pixel in the area covered by the mesh. Within this formalism, the pixel integration simply writes as a scalar product between such two vectors.

### 2.2. The original I-MIC approach

Starting from two grey level images,  $f$  and  $g$ , of the surface of a loaded sample, the original I-MIC method is written as follows: given  $f$  the image at the unloaded state and  $g$  the image under loading, the displacement field and the material parameters are obtained through the minimization of

$$\{\mathbf{U}, \Lambda\} = \text{Arg Min} \left( \frac{1}{m_o} \{\mathbf{F} - \mathbf{G}(\mathbf{U}, \Lambda)\}^T \{\mathbf{F} - \mathbf{G}(\mathbf{U}, \Lambda)\} + \left( \frac{1}{\alpha} - 1 \right) \frac{1}{k_o} \{\bar{\mathbf{F}}_{int}(\mathbf{U}, \Lambda)\}^T \{\bar{\mathbf{F}}_{int}(\mathbf{U}, \Lambda)\} \right). \quad (2)$$

In this equation, the finite element decomposition presented previously is adopted so that the nodal displacement vector  $\mathbf{U}$  is searched for.  $\mathbf{F}$  and  $\mathbf{G}$  are the vectors collecting the grey level values of the images.  $\Lambda$  is the vector that collects the values of the material parameters to identify.  $\bar{\mathbf{F}}_{int}$  is the vector that collects the internal forces for each DOF except those supported by the nodes that are concerned with Dirichlet boundary conditions or that are submitted to non-zero Neumann conditions.  $m_o$  and  $k_o$  are normalization constants that allow us to mix the two contributions of Eq. (2) with the use of the penalty parameter  $\alpha$ . The first contribution (on the left of the + sign) concerns Digital Image Correlation. Its solution produces a passive advection of  $g$  that matches  $f$  properly:

$$f(\mathbf{x}_p) = g(\mathbf{x}_p + \mathbf{u}(\mathbf{x}_p)), \quad (3)$$

$\mathbf{x}_p$  giving the position of a pixel in the reference image co-ordinate system. The second contribution (on the right of the + sign) ensures that the balance of momentum equations are satisfied by the displacement field. The two residuals cannot reach their minimum for the same displacement field which is the reason why the mechanical part is used as a penalty term. The parameter  $\alpha$  provides a control of the penalization. It was shown in Réthoré et al. (2009), where this mechanical regularization was first proposed, that  $\alpha$  is related to the cut-off wave length of the mechanical filtering provided by the penalty term. The short wave lengths of the displacement solution are dominated by the mechanical contribution

whereas the large wave lengths remain governed by the DIC contribution.

Let us note that neither the knowledge of the external load applied to the sample nor displacement boundary conditions are required in this strategy. It has been shown to be a great advantage because the response of the method is robust with respect to the noise that can affect the displacement field on the boundary. It is also important to note that this strategy does not involve static quantities, *i.e.*, external loads are not used in this approach. Of course, the global response of the specimen that should correspond to these external loads, can be estimated *a posteriori* from the displacement field and the material parameters. The ratio between the estimated and the actual loads can be used to calibrate model parameters such as Young's modulus. I-MIC has been successfully used for estimating Poisson's ratio or damage law parameters in Réthoré (2010).

The extension of the method to non-linear constitutive models, such as elasto-plasticity, is not straightforward because of the specificity detailed in the previous paragraph. Roughly speaking, if an elastic–plastic numerical simulation is run with only Dirichlet boundary conditions, then the parameters of the elastic–plastic constitutive law have a very small influence on the displacement field and conversely the loads resulting from the applied displacements change strongly. This is the reason why the initial I-MIC strategy fails in such cases. We will describe in the next section how we can modify the I-MIC approach in order to make it suitable for the identification of constitutive parameters of more general material laws, the examples of the paper focusing on elasto-plasticity.

### 2.3. The modified I-MIC approach

From the previous observation, it is clear that static quantities, *e.g.*, external loads, must be invoked by the identification strategy if we want to estimate the parameters of an elastic–plastic constitutive law. First the new I-MIC formulation is described, then details are provided on the important steps of the methodology. For the sake of clarity, we first focus on a two-dimensional case where only one deformed image coming from one camera is available.

In the original I-MIC formulation (Réthoré, 2010), the mechanical constraints were obtained by the Equilibrium Gap Method (see, *e.g.*, Claire et al., 2004; Réthoré et al., 2009) as shown in Eq. (2). It does not involve the contribution of the boundary nodes. It has been shown to be an advantage in some cases by Réthoré (2010), but as said in the previous paragraph, this specificity is the reason why the approach fails for more general constitutive laws. Keeping in mind that the experimental tests are not perfect, the external loads applied on the non-free boundary of the specimen is *a priori* unknown. We suppose that we can estimate the nodal force distribution and its amplitude (a dedicated procedure will be described later on). Then, the mechanical constraints in Eq. (2) is now formulated in a more standard way in the scope of numerical analysis. Instead of using the norm of  $\bar{\mathbf{F}}_{int}$ , a balance between the work of the external forces, collected in  $\mathbf{F}_{ext}$ , and the internal work is adopted:

$$\{\mathbf{U}, \Lambda\} = \text{Arg Min} \left( \frac{1}{m_o} \{\mathbf{F} - \mathbf{G}(\mathbf{U}, \Lambda)\}^T \{\mathbf{F} - \mathbf{G}(\mathbf{U}, \Lambda)\} + \left( \frac{1}{\alpha} - 1 \right) \frac{1}{k_o} \{\mathbf{U}\}^T \{\mathbf{F}_{ext} - \mathbf{F}_{int}(\mathbf{U}, \Lambda)\} \right). \quad (4)$$

Looking at the previous equation, we can observe that at least the optical part of the residual has a non-linear dependence on  $\mathbf{U}$ . An iterative resolution strategy is therefore employed. If  $d\mathbf{U}$  is the solution increment between two successive iterations, we have:

$$\{\mathbf{G}(\mathbf{U} + d\mathbf{U}, \Lambda)\} = \{\mathbf{G}(\mathbf{U}, \Lambda)\} + [\nabla\mathbf{G}]^T[\mathbf{N}]\{d\mathbf{U}\} \quad (5)$$

and

$$\{\mathbf{F}_{int}(\mathbf{U} + d\mathbf{U}, \Lambda)\} = \{\mathbf{F}_{int}(\mathbf{U}, \Lambda)\} + \left[\frac{\delta\mathbf{F}_{int}}{\delta\mathbf{U}}\right]\{d\mathbf{U}\}. \quad (6)$$

Introducing these expressions in Eq. (4), the stationarity with respect to  $d\mathbf{U}$  is used to obtain

$$[\mathbf{M}_{I-MIC}]\{d\mathbf{U}\} = \{\mathbf{b}_{I-MIC}\}, \quad (7)$$

where

$$\begin{aligned} [\mathbf{M}_{I-MIC}] &= \frac{1}{m_o} [\mathbf{N}]^T [\nabla\mathbf{F}] [\nabla\mathbf{F}] [\mathbf{N}] + \left(\frac{1}{\alpha} - 1\right) \frac{1}{k_o} [\mathbf{K}] \\ &= \frac{1}{m_o} [\mathbf{M}_{DIC}] + \left(\frac{1}{\alpha} - 1\right) \frac{1}{k_o} [\mathbf{K}], \end{aligned} \quad (8)$$

and

$$\begin{aligned} \{\mathbf{b}_{I-MIC}\} &= \frac{1}{m_o} [\mathbf{N}]^T [\nabla\mathbf{F}]\{\mathbf{F} - \mathbf{G}\} + \left(\frac{1}{\alpha} - 1\right) \frac{1}{k_o} \{\mathbf{F}_{ext} - \mathbf{F}_{int}\} \\ &= \frac{1}{m_o} \{\mathbf{b}_{DIC}\} + \left(\frac{1}{\alpha} - 1\right) \frac{1}{k_o} \{\mathbf{F}_{ext} - \mathbf{F}_{int}\}. \end{aligned} \quad (9)$$

In these equations, a modified algorithm is adopted: we substitute  $\nabla\mathbf{G}$ , which depends on the current solution vector  $\mathbf{U}$ , by  $\nabla\mathbf{F}$  and  $\frac{\delta\mathbf{F}_{int}}{\delta\mathbf{U}}$  is denoted by  $\mathbf{K}$  which should be the algorithmic consistent tangent matrix for optimal convergence. Note also that these definitions involve, for the optical part, the matrix  $\mathbf{M}_{DIC}$  and vector  $\mathbf{b}_{DIC}$  that can be obtained by a standard DIC problem. Once the displacement solution is obtained for a fixed value of the material parameters, we can derive the solution procedure to evaluate the material parameters increment.

In practice, a strong reduction of the internal forces is obtained, meaning that the emphasis is on the mechanical part of the cost function. The mechanical residual vanishes even for non optimal constitutive parameters. This means that the variation of  $\Lambda$  can only influence the optical part of the cost function. The solution increment for the constitutive parameters is obtained by minimizing the DIC residual only. For this purpose, we use

$$[\mathbf{M}_\Lambda]\{d\Lambda\} = \{\mathbf{b}_\Lambda\}. \quad (10)$$

In this equation, the following definitions hold:

$$[\mathbf{M}_\Lambda] = \left[\frac{\Delta\mathbf{U}}{\Delta\Lambda}\right]^T [\mathbf{N}]^T [\nabla\mathbf{F}] [\nabla\mathbf{F}] [\mathbf{N}] \left[\frac{\Delta\mathbf{U}}{\Delta\Lambda}\right] = \left[\frac{\Delta\mathbf{U}}{\Delta\Lambda}\right]^T [\mathbf{M}_{DIC}] \left[\frac{\Delta\mathbf{U}}{\Delta\Lambda}\right] \quad (11)$$

and

$$\{\mathbf{b}_\Lambda\} = \left[\frac{\Delta\mathbf{U}}{\Delta\Lambda}\right]^T [\mathbf{N}]^T [\nabla\mathbf{F}]\{\mathbf{F} - \mathbf{G}(\Lambda)\} = \left[\frac{\Delta\mathbf{U}}{\Delta\Lambda}\right]^T \{\mathbf{b}_{DIC}\}, \quad (12)$$

the sensitivity matrix  $\frac{\Delta\mathbf{U}}{\Delta\Lambda}$  being computed with  $\mathbf{U}$  fields that are obtained by solving Eq. (7). The process is run until convergence is reached on  $\Lambda$  for a given criterion  $\eta$  and a given limit  $\eta_c$ . In practice, the maximum of the ratio between the parameter increment and its current value is used.

$$\eta = \text{Max} \frac{\delta\Lambda}{\Lambda}. \quad (13)$$

The convergence tolerance  $\eta_c$  is set to  $10^{-3}$ . In Réthoré (2010), the sensitivity to image noise of the original I-MIC strategy is derived, and it is further shown that the approach is optimal. The modified strategy proposed here shares strong similarities with the original one. Indeed, following the analysis in Réthoré (2010), we can show that there is no systematic bias. We obtain a covariance matrix of the perturbation of the constitutive parameters due to image noise expressed as follows

$$\langle\langle\{\delta\Lambda\}\{\delta\Lambda\}^T\rangle\rangle = 2 \left[ \left[\frac{\Delta\mathbf{U}}{\Delta\Lambda}\right]^T [\mathbf{M}_{DIC}] \left[\frac{\Delta\mathbf{U}}{\Delta\Lambda}\right] \right]^{-1} \sigma^2. \quad (14)$$

In this equation,  $\langle\langle\bullet\rangle\rangle$  is the average operator over the realizations of  $\bullet$ ,  $\sigma$  is the standard deviation of the image noise, a white noise being considered. The expression in Eq. (14) is the same as the one for the original I-MIC in Réthoré (2010). The only difference is that we assume that there is no noise affecting the external force vector  $\mathbf{F}_{ext}$ . Of course, this is not the case in practice. However, it will be shown in the example section that this noise has a negligible contribution.

### 3. Integrated mechanical image correlation using 3D kinematics (I-MIC3D)

The present paper is devoted to the identification of the parameters of elastic-plastic constitutive laws. Due to plastic incompressibility, three dimensional effects play an important role. As we do not want to restrict the analysis to thin sheets, an extension of the approach to three-dimensional kinematics is proposed. For this purpose, the DIC mesh is extruded along the mean normal direction of its surface so that the mechanical part of the I-MIC functional is computed in 3D. We will first detail how this operation is performed depending on the number of cameras and then the identification strategy will be presented.

#### 3.1. Using a single camera

A mesh of the specimen in the physical space (*i.e.*, using physical units) is first generated. Using simple affine transformations this mesh is glued on the reference image so that its contour coincides with the contour of the specimen. The DIC analysis is performed without further mesh modification except mesh refinement if needed. The direction normal to the sample surface is supposed to be orthogonal to the camera sensor plane. The 2D mesh is simply extruded along this direction. The thickness of the specimen is converted from physical units into pixels. This mesh will be used for the 3D numerical integration of the mechanical operator  $\mathbf{K}$  and  $\mathbf{F}_{int}$  whereas only the projection of the first node layer onto the sensor plane is accounted for in the integration of the correlation operator  $\mathbf{M}_{DIC}$  and  $\mathbf{b}_{DIC}$ . A projection operator is defined such that the projected displacement reads

$$\{\mathbf{U}_p\} = [\mathbf{P}]\{\mathbf{U}\}, \quad (15)$$

where  $\mathbf{P}$  is a diagonal matrix. The  $i$ th diagonal term  $P_i$  is zero if the corresponding DOF is held by a node not located on the first layer. Otherwise its value is set to unity if the corresponding DOF has its component within the sensor plane.

#### 3.2. Using two or more cameras

The same methodology is now derived for stereo-correlation, or multiple camera correlation system. The main difference is that the analysis is performed in the physical space but not within the sensor space. First a 2D mesh is positioned within the physical space so that its projections on the images of the two cameras match the projection of the specimen. Then the 3D displacement is projected onto the sensors of the two cameras and the correlation residuals are computed. The projection operator is different for each camera, it will be denoted as  $\mathbf{P}_c$  of the  $c$ th camera.

#### 3.3. Problem formulation

In the following, we will analyze a sequence of images captured all along the sample loading. The modified I-MIC3D functional is

adapted for the case of multiple images coming from multiple cameras in the following way:

$$\begin{aligned} \{\mathbf{U}, \Lambda\} = \text{Arg Min} & \left( \left( \frac{1}{\alpha} - 1 \right) \frac{1}{k_0} \sum_{t=0}^T \{\delta \mathbf{U}\}^T \{\mathbf{F}_{ext}(t) - \mathbf{F}_{int}(\mathbf{U}, \Lambda)\} \right. \\ & + \frac{1}{m_0} \sum_{c=1}^{N_{cam}} \sum_{t=0}^T \{\mathbf{F}_c(t) - \mathbf{G}_c(t, [\mathbf{P}_c]\{\mathbf{U}\}, \Lambda)\}^T \{\mathbf{F}_c(t) \\ & \left. - \mathbf{G}_c(t, [\mathbf{P}_c]\{\mathbf{U}\}, \Lambda)\} \right). \end{aligned} \quad (16)$$

In this equation, a subscript  $c$  has been added to the image vector to indicate the camera number. Discrete summation over time and over the cameras has also been added in order to generalize the functional (4) that is dedicated to one image coming from one camera. The work of the internal and external forces is substituted by the sum over time of the power of these forces,  $\delta \mathbf{U}$  being the increment over time of the displacement vector.

### 3.4. Numerical features

An elastic plastic constitutive model up to large deformation is tracked for in this paper. The mechanical part of the I-MIC3D functional is written considering geometrical non-linearities in an updated-Lagrangian framework. In addition, the numerical integration of the internal force vector is performed using a reduced integration strategy. When performing numerical simulations using finite elements with reduced integration, one has to control zero-energy hourglass deformation modes. In the present case, the optical part of the functional controls these modes and there is no need to introduce artificial forces.

The I-MIC3D functional proposed herein involves the finite element external force vector  $\mathbf{F}_{ext}$ . This vector is *a priori* unknown, only its resultant being measured experimentally. In practice, we elaborate the following strategy. Given the initial guess of the material parameters and the displacement field obtained by solving a pure DIC problem, a “direct” numerical simulation is performed using this displacement field as boundary conditions and the initial constitutive parameters. From this direct numerical simulation, an external force vector  $\mathbf{F}_{ext}^0$  can be computed in a post-processing step as the reaction forces to the prescribed displacement field. This gives us a distribution of nodal forces that allows to obtain a realistic displacement field since the pure DIC displacement was prescribed on the mesh boundary. The resultant of  $\mathbf{F}_{ext}^0$  is calculated and then scaled so that it equals the experimental resultant force. By multiplying  $\mathbf{F}_{ext}^0$  by this scaling factor, a realistic nodal force distribution  $\mathbf{F}_{ext}$  which resultant is equal to the experimental force measurement is obtained and used in the I-MIC3D functional.

## 4. Virtual testing

In this Section, a virtual testing procedure is elaborated in order to estimate the performance of the proposed identification strategy. The principle is the following: given a sample geometry and the constitutive law, a numerical simulation is performed, then the mesh is glued onto a virtual image (that can be synthetic or not) and this image is deformed according to the computed displacement field and virtually deformed images are generated. Fig. 1 shows the main steps of the virtual testing procedure used herein. Given  $f$  the reference image, we generate  $g$  so that for a given displacement field  $\mathbf{u}$  we have

$$f(\mathbf{x}_p) = g(\mathbf{x}_p + \mathbf{u}(\mathbf{x}_p)). \quad (17)$$

In this equation,  $\mathbf{x}_p$  are integer pixel positions. In practice, we want the argument of  $g$  to be integer values. The mapping  $\Phi(\mathbf{x}_p) = \mathbf{x}_p + \mathbf{u}(\mathbf{x}_p) = \mathbf{X}$ , where  $\mathbf{X}$  are non-integer position, is in-

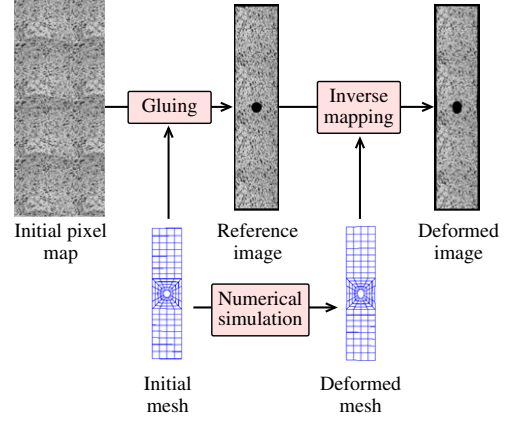


Fig. 1. Illustration of the virtual testing procedure.

verted:  $\mathbf{x} = \Phi^{-1}(\mathbf{X}_p)$  so that  $g$  is computed at integer pixel position as a sub-pixel interpolation of  $f$ . Given integer pixel position  $\mathbf{X}_p$ , non-integer position  $\mathbf{x}$  are searched for so that  $\mathbf{x} + \mathbf{u}(\mathbf{x}) = \mathbf{X}_p$ . A Newton–Raphson procedure is used to obtain  $\mathbf{x}_p$  and spline-cubic gray level interpolation is performed to compute  $g(\mathbf{X}_p) = f(\mathbf{x})$ . Once the images have been generated, the proposed identification strategy is run and we study the influence of the penalty parameter and the initial guess for the material parameters.

### 4.1. Test design

A virtual sample with a hole similar to the real one that will be studied in the next Section is considered. The sample width is 20 mm, and its thickness is 8 mm. A hole of 5 mm in diameter is machined in the center of the sample. The material considered in the numerical simulation for the virtual testing has an elastic–plastic behavior. For the elastic regime, the parameters are Young’s modulus  $E$  and Poisson’s ratio  $\nu$  which values are set to 198 GPa and 0.25, respectively. For the plastic regime, a nonlinear isotropic hardening is considered. The evolution of the yield stress  $\sigma_y$  as a function of the accumulated plastic strain  $\varepsilon_p$  is parametrized as follows:

$$\sigma_y(\varepsilon_p) = H \varepsilon_p + S_y \left( 1 + \frac{\varepsilon_p}{\varepsilon_0} \right)^\delta. \quad (18)$$

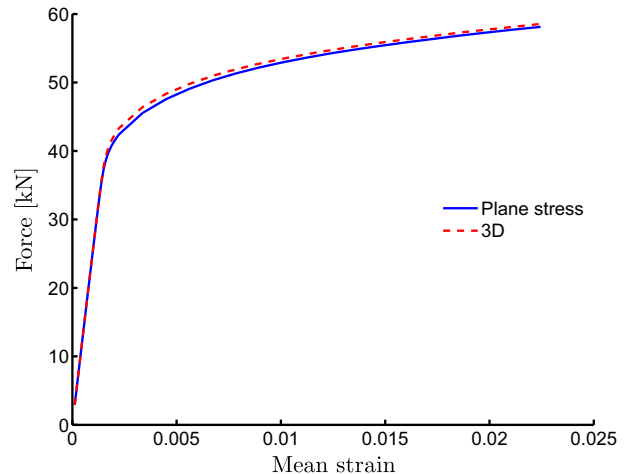
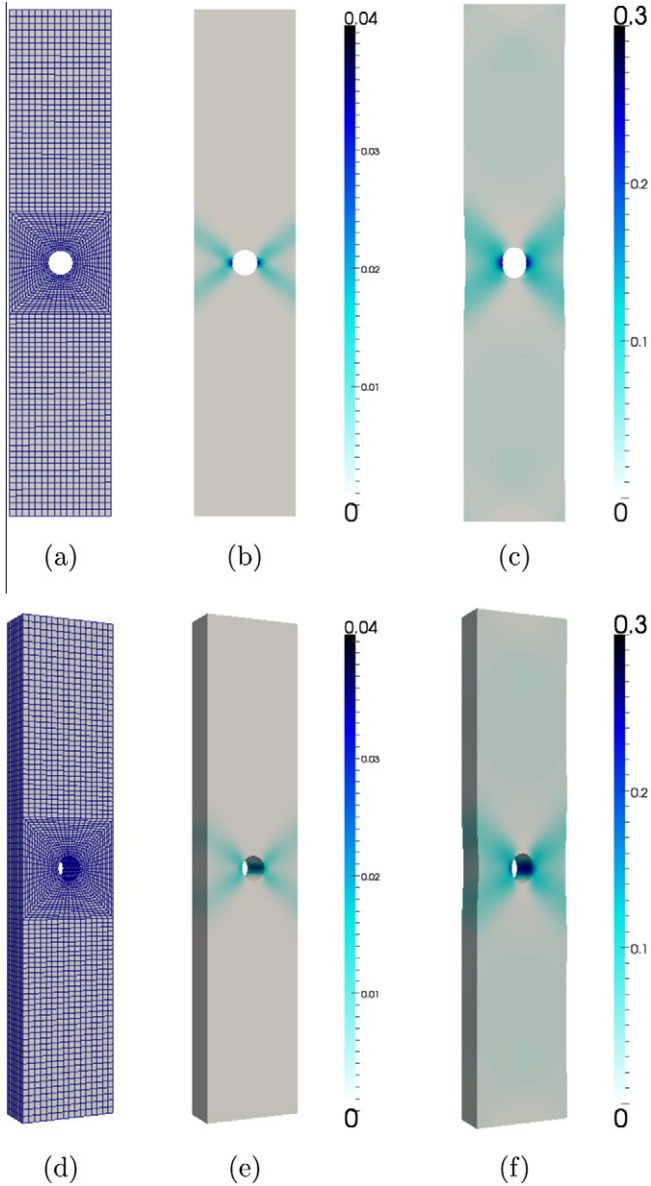
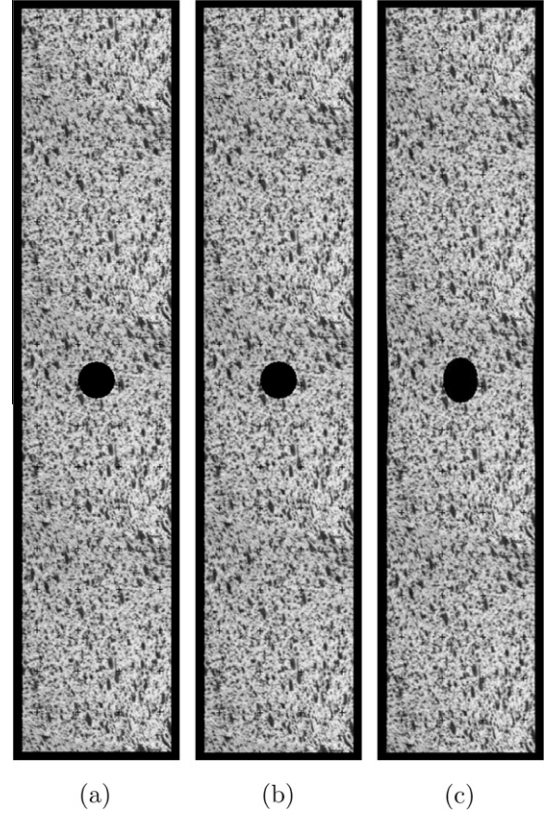


Fig. 2. Global response (force v.s. mean strain curve) of the virtual tests in plane stress or in 3D.



**Fig. 3.** Mesh and accumulated plastic strain distribution for the virtual test. Figures (a) and (d) show the mesh used for the plane stress and 3D analysis, respectively. Figures (b) and (e) the accumulated plastic strain distribution at stage 1 and figures (c) and (f) the same field but at stage 2.

$H$  is a linear hardening coefficient,  $S_y$  the initial yield stress and  $\varepsilon_0$  a scaling factor for the accumulated plastic strain. The respective values for the parameters are: 1480 MPa for  $H$ , 284 MPa for  $S_y$ ,  $7.16 \cdot 10^{-5}$  for  $\varepsilon_0$  and 0.042 for  $\delta$ . These constitutive parameters have been identified for the material studied in the next section using a uniaxial experiment with an extensometer. The virtual tests are performed in plane stress conditions or using full 3D analysis. Fig. 2 shows the global response of the virtual sample for both types of analysis. It is observed that there are not significant differences between the two models. The feasibility of using 3D kinematics within the proposed framework will thus be demonstrated. However the advantage of using a 3D instead of 2D plane stress will not be discussed. The numerical simulations have been carried out using the mesh shown in Fig. 3(a) and (d), respectively. In the following identification analysis, three stages will be considered: stage 0 contains all the steps before the onset of plasticity (5 images), stage 1 contains the steps for a maximum accumulated plastic strain up



**Fig. 4.** Virtual images generated for the reference state, for stage 1 and stage 2.

to 4% (20 images) and stage 2 the steps for  $\varepsilon_p$  up to 30% (40 images). Fig. 3(b) and (e) and Figs. 3(c) and (f) show the accumulated plastic strain distributions for stage 1 and stage 2. The corresponding images generated as described above are shown in Fig. 4.

#### 4.2. Identification

To avoid inconsistency in the stress/strain curve of the identified material, we prescribe that the initial tangent modulus,  $\frac{\partial \sigma_y}{\partial \varepsilon_p}(\varepsilon_p = 0)$ , equals Young's modulus  $E$ . We chose  $E, H, \delta$  and  $S_y$  as parameters to be identified, and  $\varepsilon_0$  is obtained using

$$\varepsilon_0 = \frac{\delta S_y}{E - H}. \quad (19)$$

In the following analysis several types of identification are performed. Sequential identifications, meaning that the parameters are identified one by one the other ones being fixed during the iteration. For this sequential identification strategy, not all the images may be used for the identification of all the parameters:

- identification of  $E$  using images of stage 0,
- identification of  $S_y$  using images of stage 1,
- identification of  $H$  using images of stage 2,
- identification of  $\delta$  using images of stage 2.

We have also tested simultaneous identification strategy for  $S_y$  and  $H$  or  $H$  and  $\delta$ . In this case images of stage 2 are used.

In these analysis, only the parameters to be identified are unknown and all the others parameters are set to their respective actual value. The meshes used for the I-MIC3D analysis have a lower refinement than those used for the direct analysis and the virtual images generation. In the following, we will focus on the identification of  $E, S_y$  and  $H$ .

#### 4.3. Influence of $\alpha$

We first perform sequential identification of  $E$  and  $S_y$  for different values of the penalty parameter  $\alpha$ . The initial guess for Young's modulus  $E^0$  and the initial yield stress  $S_y^0$  are set to 90% of their actual value. The influence of  $\alpha$  on the identified value for  $E$  and  $S_y$  is shown in Fig. 5 where  $\bar{E}$  and  $\bar{S}_y$  are the ratio between the current parameter value and its actual value are plotted. Starting from value of  $\alpha$  close to 1 (where the emphasis is on the DIC part of the functional), the result progressively improves when  $\alpha$  decreases. For  $\alpha = 10^{-4}$ , the relative error on  $E$  is 0.15% and 0.62% on  $S_y$ . From our experience and as demonstrated by the curves in Fig. 5, one may chose  $\alpha$  as small as possible. The limit when  $\alpha$  vanishes of the I-MIC strategy consists in performing "direct" numerical simulation under prescribed forces and to minimize the DIC part of the functional with respect to the material parameters (see also Leclerc et al., 2009 and Réthoré, 2010). This limit case will be used in the rest of the paper as it is more efficient in terms of accuracy as well as computational cost. In this case the relative errors are 0.11% for  $E$  and 0.12% for  $S_y$ .

#### 4.4. Influence of initial guess

Optimization techniques may be sensitive to the initial guess for the searched parameters. In the present strategy, this initial guess may not only affect the convergence of the optimization algorithm but also the estimation of the external force vector as explained in Section 3.4. In this respect, this is essential to evaluate the robustness of the proposed approach with respect to the initial parameter values.

For plane stress calculations and full 3D analysis, Fig. 6 shows the evolution of the identified parameters using a sequential strategy when the initial guess varies from 80% to 120% of the actual parameter value. For Young's modulus the mean deviation is 0.15% for plane stress and 0.07% for 3D. Concerning its standard deviation we obtain 0.009% and 0.012%, respectively. For the initial yield stress we have 0.12% for the systematic error in plane stress and 0.017% as standard deviation. For the 3D case, we obtain 0.16% and 0.017%, respectively. These values are really low and they demonstrate that the proposed method has a really low sensitivity to the initial parameter value. The results are a little less accurate concerning the linear hardening modulus, which probably has a lower influence on the solution. The systematic error is 0.9% for a standard deviation of 0.045% in plane stress whereas for 3D

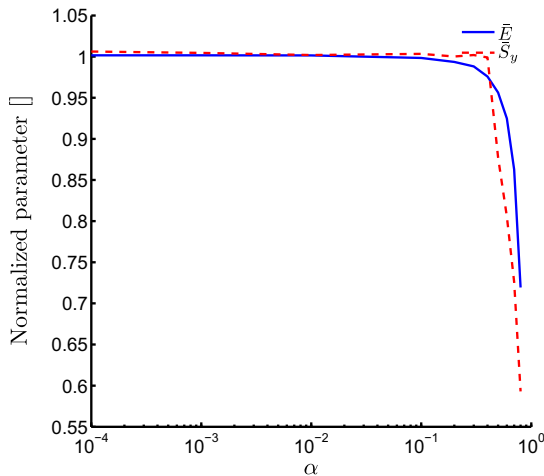


Fig. 5. Influence of the penalty parameter  $\alpha$  for identification of type I and II in plane stress.

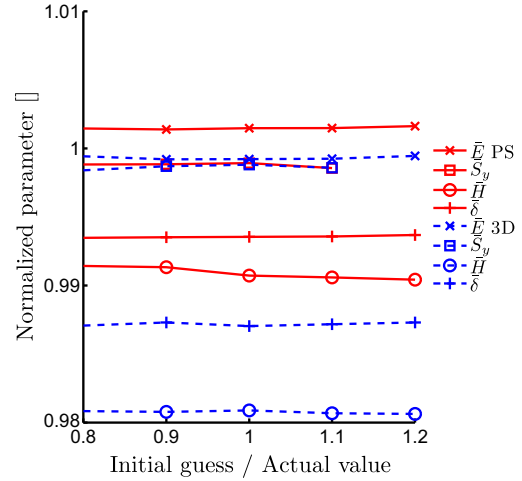


Fig. 6. Influence of the initial guess for sequential identification based on plane stress assumption or on full 3D kinematics.

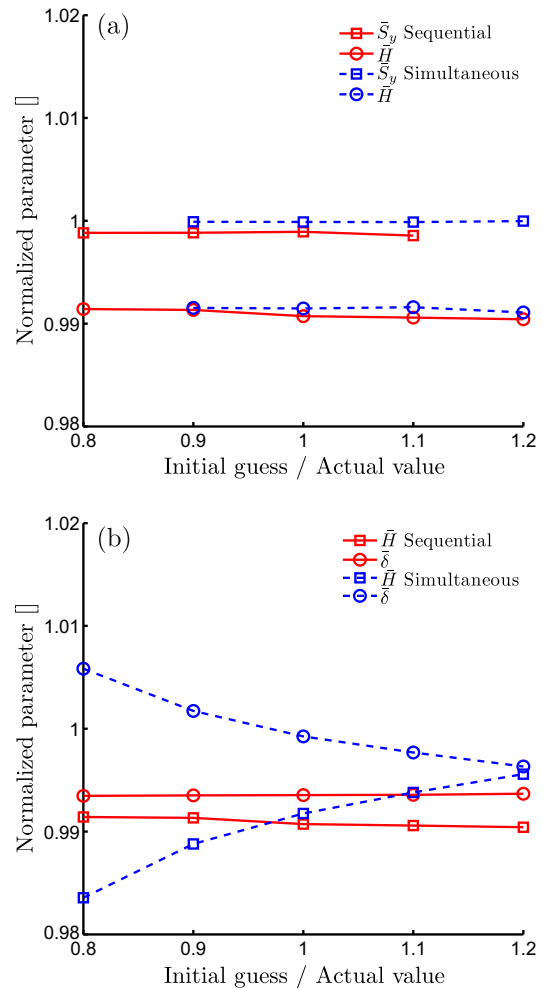
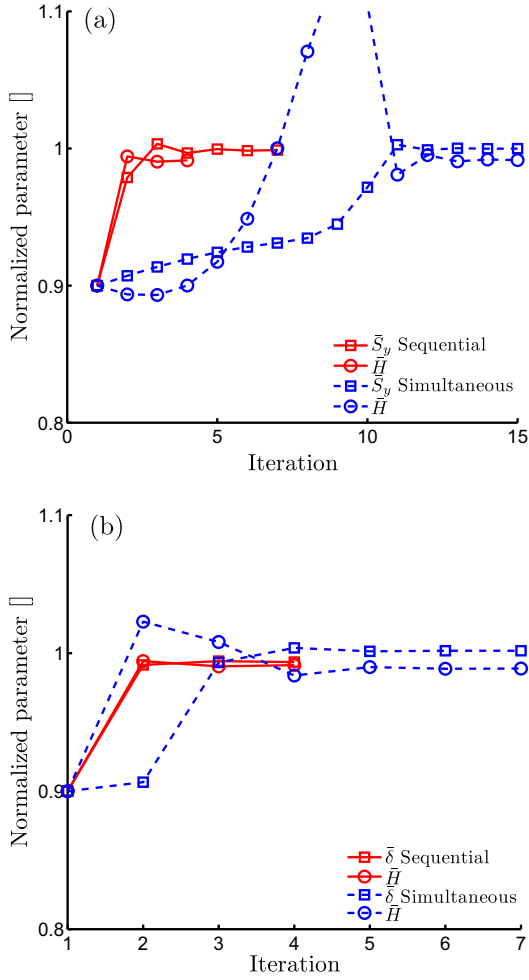


Fig. 7. Influence of the initial guess for identification based on plane stress assumption. Results for sequential identification or simultaneous identification of parameter pairs  $(S_y, H)$  or  $(H, \delta)$  are presented.

we obtain 1.9% and 0.01%, respectively. However, the estimated values are within a range of the order or lower than 1% which can be considered as extremely robust. The hardening exponent



**Fig. 8.** Evolution of the identified parameters of sequential or simultaneous identification of parameters pairs  $(S_y, H)$  or  $(H, \delta)$  based on plane stress assumption during the iterations. The initial guess for both parameters is 90% of the actual parameter value.

$\delta$  is identified with very low error: in plane stress the systematic error is 0.6% for a standard deviation of 0.008% whereas of 3D we get 1.3% and 0.012%, respectively.

In Fig. 7, the results obtained from sequential and simultaneous identifications are compared, *i.e.*, for a two steps identification or a simultaneous identification of parameter pairs: the initial yield stress and the linear hardening coefficient  $(S_y, H)$  or the linear hardening coefficient and the hardening exponent  $(H, \delta)$ . It is shown that similar results are obtained and that the two parameters of a pair can be estimated at the same time with the same accuracy and robustness as they were identified separately except for the pair  $(H, \delta)$  which is more efficiently identified using a sequential identification. The price for a simultaneous identification is a lower convergence speed as illustrated in Fig. 8. Indeed in Fig. 8(a), for a sequential identification, 7 then 4 iterations are required for  $S_y$  and  $H$ , respectively whereas convergence is achieved for a simultaneous identification after 15 iterations. Moreover, simultaneous identification, the analysis are performed over all the 40 images whereas for sequential identification of  $S_y$  only involves the first 20 ones. The cost of sequential identification is thus even less expensive. The same conclusions arise from Fig. 8(b) for the pair  $(H, \delta)$ . However, it is demonstrated that both hardening parameters can be identified at the same (*i.e.*, using a simultaneous identification) using the proposed method.

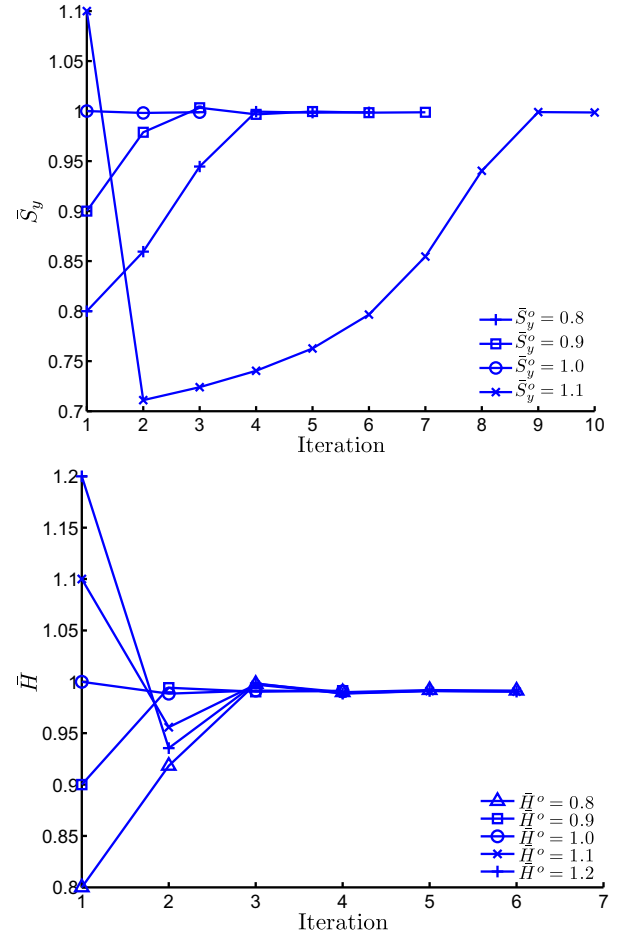


**Fig. 9.** Evolution of the identified parameters of sequential identification based on plane stress assumption during the iterations for various values of the initial guess.

The convergence speed of the method is illustrated in Fig. 9 for sequential identification and in Fig. 10 for simultaneous identification. For different values of the initial parameter guess, the evolution of the estimated parameter is plotted. We focus on  $S_y$  and  $H$  under plane stress. We can observe that except for  $S_y$  with an initial guess of 110% of the actual value, the convergence of sequential identification is very fast: only 3 or 4 iterations are required for an acceptable estimation of the parameter. However, for this case ( $S_y$  with an initial guess of 110%), under-relaxation should have been adopted so that the parameter increment at the first iteration is smaller and the convergence faster. The convergence for simultaneous identification is slower. However acceptable values of the parameters are obtained within 10 iterations.

The performance of the proposed identification method that is based on DIC concept can also be appreciated by examining the evolution of the mean correlation error. For a plane stress analysis and a sequential identification of  $H$ , Fig. 11(a) shows the overall mean correlation error as a function of the iteration for different value of the initial parameter guess. This graph shows that when the initial guess spreads from the actual parameter value, the initial value of the error increases. However, during the iterations it decreases rapidly to the minimum value of 1.8% of the image dynamic. Fig. 11(b) shows the evolution of the mean correlation error with respect to the mean strain for the converged value of the parameter. The mean error is plotted as a function of the mean strain for the converged parameter value. This evolution is compared to the result from a pure DIC analysis. We can see that for very low mean strain (below 0.5%) the error for I-MIC and DIC

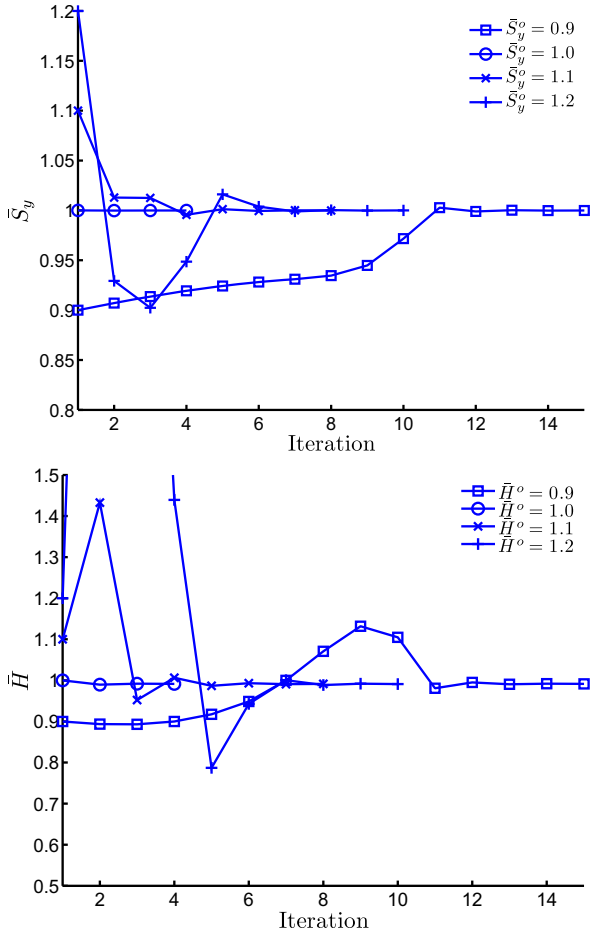


**Fig. 10.** Evolution of the identified parameters of simultaneous identification of  $S_y$  and  $H$  based on plane stress assumption during the iterations for various values of the initial guess.

are similar. When the mean strain increases, the error for I-MIC becomes higher than the error for DIC. The increase in the correlation error is not due to an incorrect estimation of the material parameter: in the present case the relative error in the estimated parameters is of 0.83%. Indeed, if the material parameter were estimated exactly the overall mean correlation would be 1.79% of the image dynamic. This value being really close to the one obtained with the identified value of the material parameter, the fact that the correlation error for I-MIC deviates from the error for pure DIC comes from the boundary conditions and the estimated external force vector. The boundary conditions applied in the I-MIC analysis are obtained from DIC. They thus deviate from the actual boundary condition applied the simulation used to generate the images. This difference explains why even for the exact constitutive parameter value, the correlation residual for I-MIC is higher than for DIC.

The virtual testing procedure proposed in this Section provides meaningful information concerning the performance of the proposed I-MIC method in terms of convergence and robustness. It allows to test different identification strategies (sequential or simultaneous). As illustrated, sequential identification offers more accuracy in the identified parameters and faster convergence. For the real experiment analyzed in the next Section, only this strategy is used. A key point for the application of the method to real experiments is that there is an increase of the correlation error compared to pure DIC due to the fact that the DIC displacement field does not satisfy the balance of momentum equation. If such

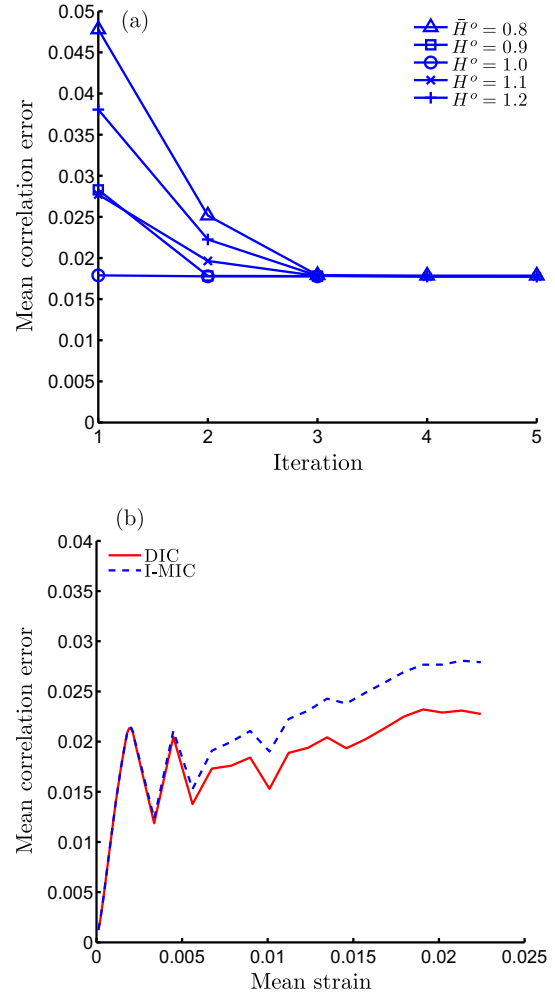


**Fig. 11.** Evolution of overall mean correlation error (normalized by the dynamic of the image) (a) for sequential identification of  $H$  based on plane stress assumption during the iterations and (b) mean correlation error as a function of the mean strain when convergence on the constitutive parameter is achieved. The correlation error obtained by a DIC analysis is also plotted. The initial parameter guess is 90% of the actual parameter value.

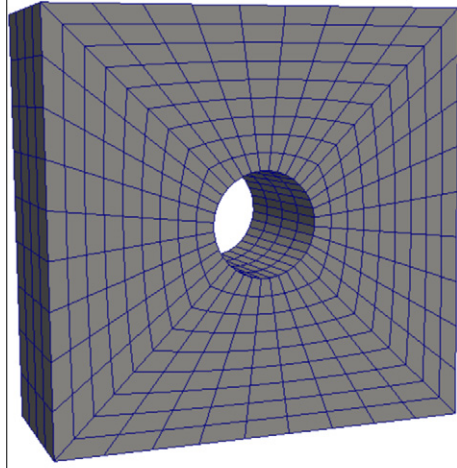
a condition is prescribed, which is the case using I-MIC, there is an increase of the correlation error. Uncertainties in the boundary conditions may further increase this error.

## 5. Example

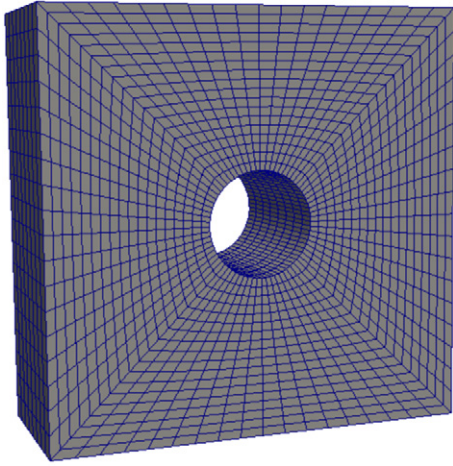
### 5.1. Test setup

After virtual tests were performed on the sample analyzed in the previous section, actual experiments are carried out. The sample has the same geometry as described previously and the idealized loading conditions are also the same. The material is a 304L stainless steel. A uniaxial test was first performed and the material parameters identified by exploiting the force/displacement curve. The material model is the same as previously and the values of the material parameter identified with the uniaxial experiment are the ones that were used in the previous section. As for the virtual test, two mesh refinements will be tested in the analysis. The 3D meshes, mesh 0 and mesh 1 are depicted on Fig. 12.

The global response of the sample is presented in Fig. 13. Stage 0 contains all the steps before the onset of plasticity (5 images,  $F \leq 20$  kN), Young's modulus  $E$  will be identified using these



(a) Mesh 0



(b) Mesh 1

Fig. 12. Meshes used for the identification.

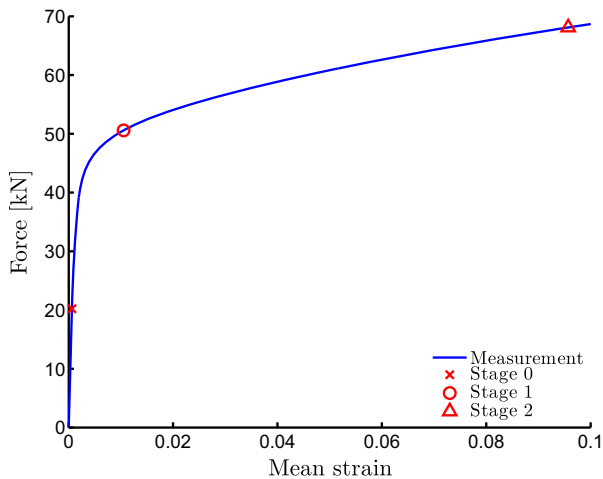
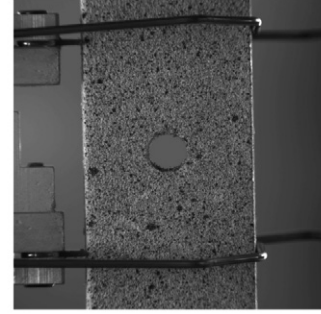


Fig. 13. Global response (force v.s. mean strain curve) of the real experiment. The different stages for the sequential identification of the material parameters are also defined on this graph.

images. Stage 1 contains the steps for low plastic strain (12 images,  $F \leq 50$  kN), the initial yield stress  $S_y$  will be identified with this



(a)



(b)



(c)

Fig. 14. Reference images for the real experiment. The image using one camera with a telecentric is (a). (b) and (c) are respectively the reference images for the left and right camera of the stereo-vision system.

data. For the identification of  $H$  and  $\delta$ , stage 2 contains the steps for  $\epsilon_p$  up to 30% (70 images,  $F \leq 68$  kN). A mean strain value is measured during the experiment using the extensometer shown in Fig. 14.

### 5.2. DIC analysis

In this section, real images acquired during a real experiment are analyzed. On one side of the sample a  $2048 \times 2048$  pixels digital camera mounted with a telecentric lens is used. The physical size of a pixel is  $18 \mu\text{m}$ . The telecentric lens allows to capture images of the sample's surface without any influence of the out of plane displacement. Thus, only in-plane displacement can be captured by DIC. However the mechanical model for the I-MIC3D analysis is 3D in order to account for out of plane effect obtained because of the finite thickness of the sample and plastic incompressibility. On the other side of the sample, two cameras with a  $4872 \times 3248$  pixel CCD mounted with a 300 mm lens are used. The stereo-vision system is calibrated using standard procedures. The image acquisition of the three cameras is synchronized. Fig. 14 shows the reference images for the three cameras. One may notice that the field of view and the magnification is not the same for the two systems (mono and stereo). However, the number of pixels within the region of interest, a square shaped region centered at the hole, is almost the same.

The displacement field obtained by DIC and stereo-DIC are plotted in Fig. 15. The in-plane components of the displacement for the two DIC systems can be compared for the last analyzed image ( $F = 68$  kN). A quasi-exact match is obtained. Stereo-DIC also pro-

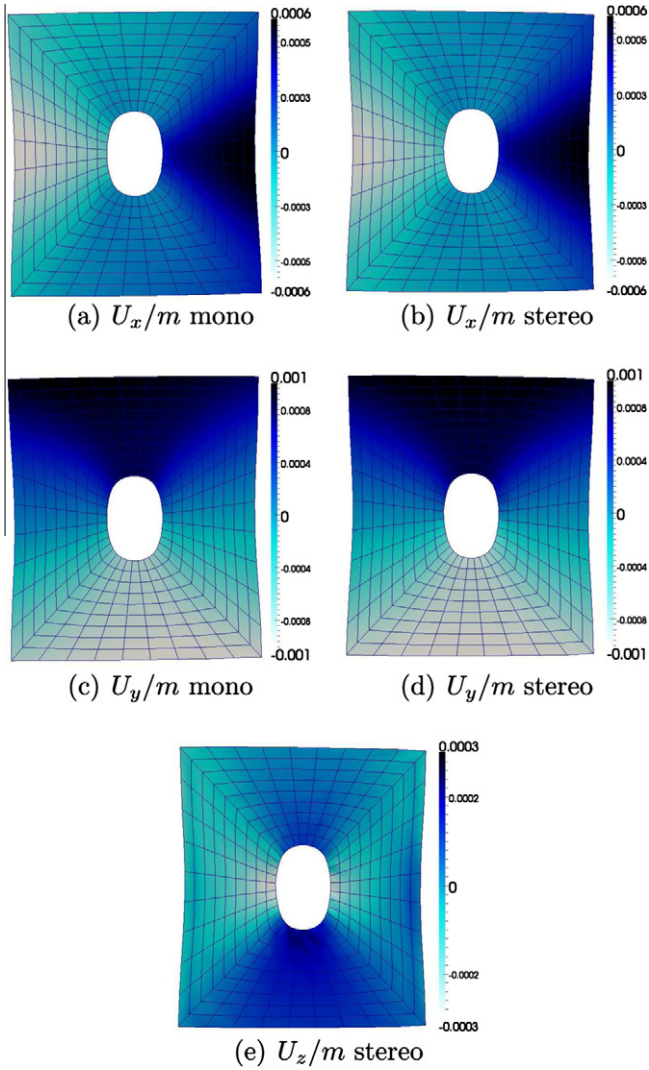


**Fig. 15.** Comparison of the displacement field obtain using mono (a, c) and stereo DIC (b, d, e). The vertical (c, d), horizontal (a, b) and out of plane (e) component of the displacement field are plotted in meter on the deformed mesh for the last analyzed image ( $F = 68$  kN).

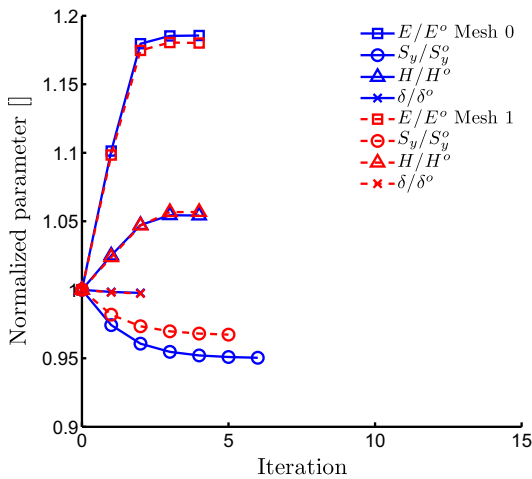


**Fig. 16.** Evolution of the identified parameters for sequential identification on the real experiment using a single camera for different mesh refinement.

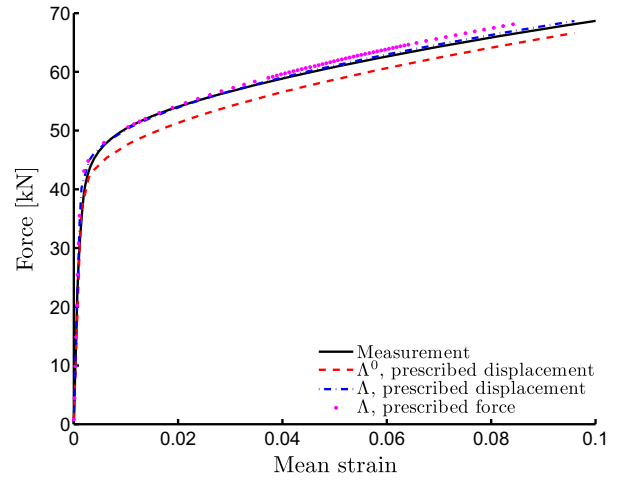


**Fig. 17.** Comparison of the load v.s. mean strain curves: experimental data and numerical results from different simulations are plotted.

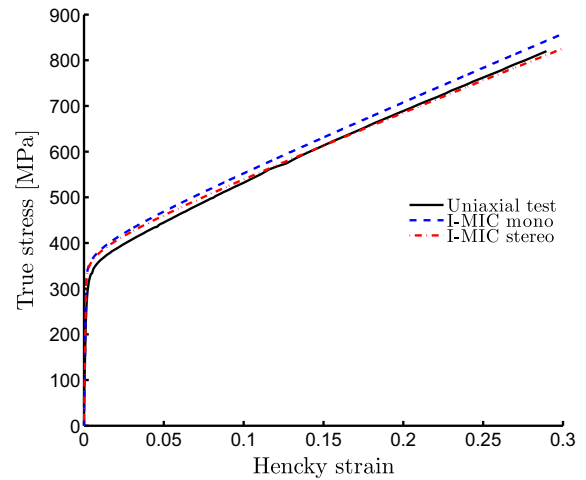


**Fig. 18.** Comparison of the stress/strain curves obtained by a uniaxial experiment and the identification using Mesh 1 and both mono and stereo camera systems.

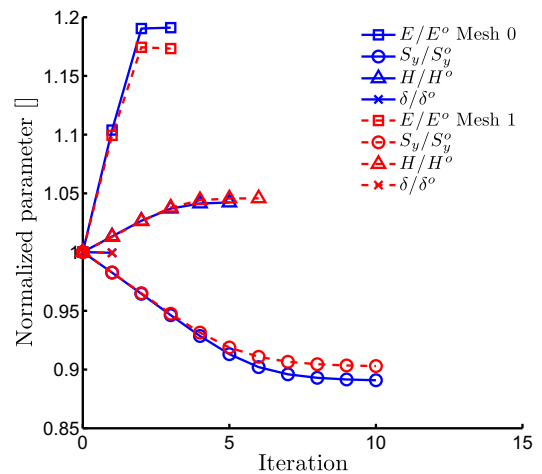


**Fig. 19.** Evolution of the identified parameters for sequential identification on the real experiment using a two camera system for different mesh refinement.

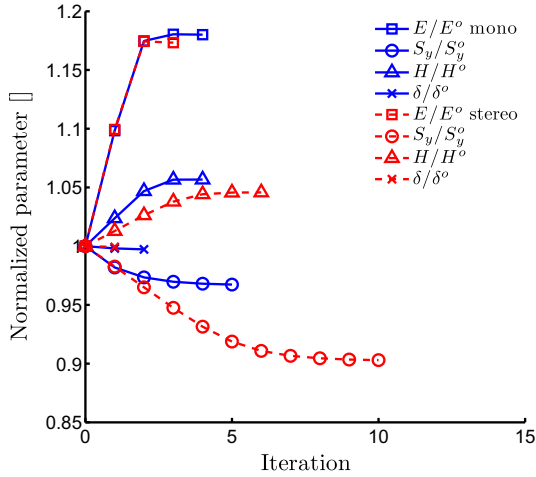


**Fig. 20.** Comparison between a single camera system or a two camera system. The evolution of the identified parameters is plotted for sequential identification on the real experiment.

**Table 1**  
Comparison of the constitutive parameters obtained using the uniaxial experiment, I-MIC 3D using a single camera or two cameras.

	Uniaxial	Mono	Stereo
$E$	198 GPa	233 GPa	232 GPa
$S_y$	284 MPa	300 MPa	297 MPa
$H$	1480 MPa	1431 MPa	1337 MPa
$\delta$	0.0420	0.0419	0.0420

vides the out of plane displacement that holds meaningful information in the present case.

### 5.3. I-MIC3D with one camera

Using the image from the single camera system, the results of the identification are presented in Fig. 16. 4 iterations are needed for the identification to converge for  $E$  and  $H$  where 5 or 6 iterations are required for  $S_y$  depending on the mesh refinement. This illustrates that the I-MIC3D formalism allows to formulate an optimization problem with a cost function that has well defined optimums. The sensibility to the mesh size is also tested. Mesh 0 is the same mesh as for DIC (as depicted in Figs. 15 and 12) but extruded along the direction normal to the initial mesh surface. For this mesh, the number of element through the thickness is 4. Mesh 1 is the same as Mesh 0 but it has been refined once in each direction. Fig. 16 shows that the identification has a negligible sensitivity to the mesh size in terms of estimated parameter value but also in terms of convergence speed. Fig. 17 allows to compare the global response of the sample (load v.s. mean strain curve) for different cases:

- experimental measurements,
- numerical simulation under prescribed displacement using the initial constitutive parameters,
- numerical simulation under prescribed displacement using the converged constitutive parameters,
- numerical simulation under prescribed force using the converged constitutive parameters.

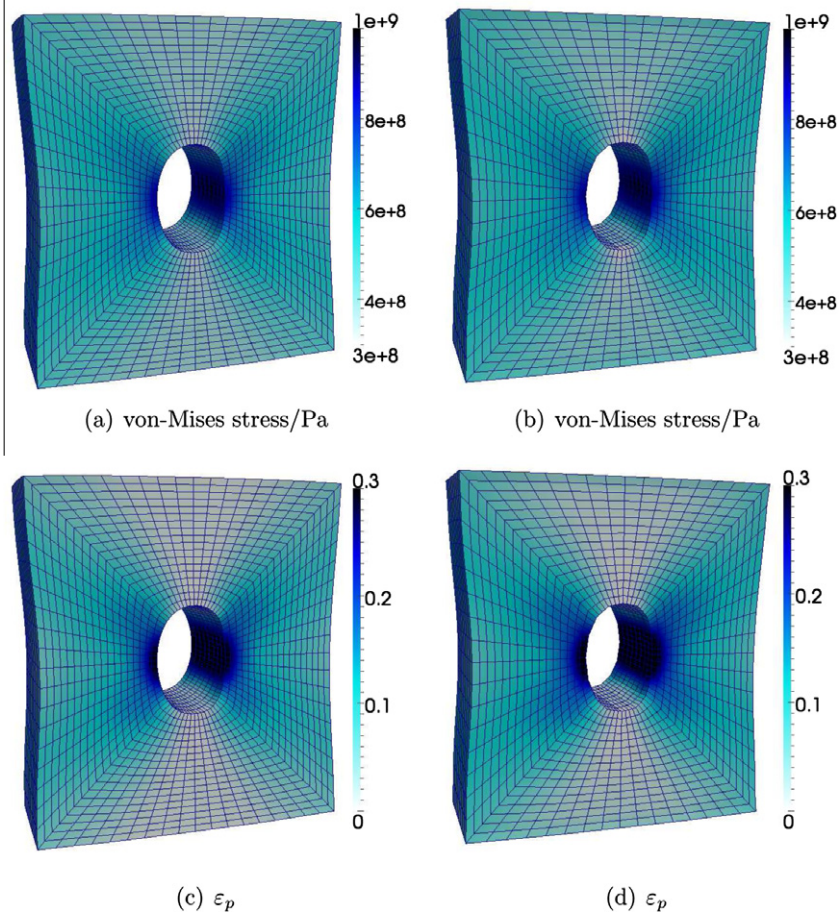


**Fig. 21.** Von-Mises stress in Pa ((a) and (b)) and accumulated plastic strain ((c) and (d)) for I-MIC analysis with Mesh 1 based on a single camera system ((a) and (c)) and a two cameras system ((b) and (d)) for the last analyzed image ( $F = 68$  kN).

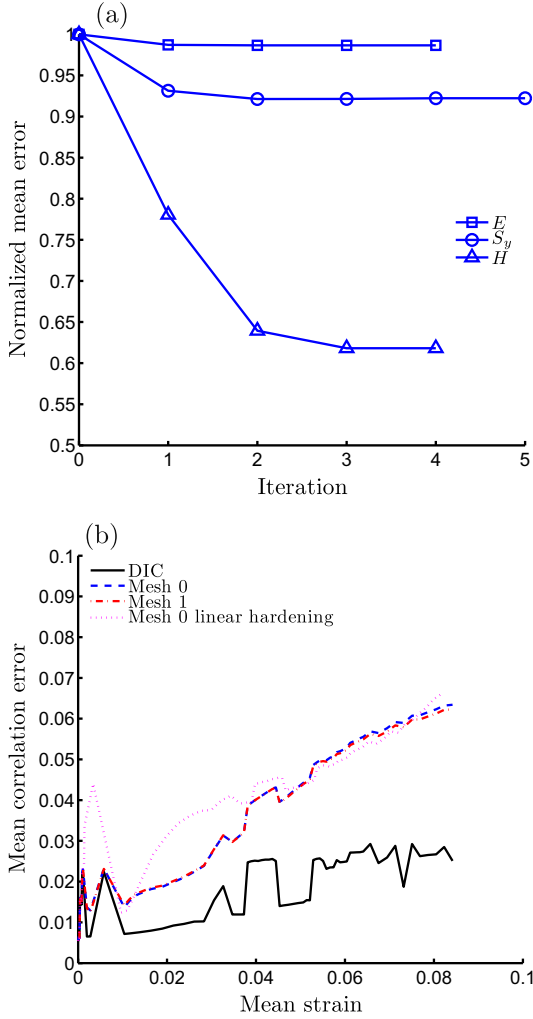


**Fig. 22.** Evolution of the overall mean correlation error (normalized by its value with the initial parameter guess) during the identification of  $E$ ,  $S_y$  and  $H$  for the single camera system with the fine mesh (a). Evolution of the mean correlation error as a function of the mean strain when convergence is achieved on the constitutive parameters (b).

For numerical simulations under prescribed displacement, the DIC displacement is imposed. For numerical simulations under prescribed forces the external force vector obtained as detailed in Section 3.4 is used. Those numerical simulations are run using Mesh 1. It is shown that the numerical simulation under prescribed displacement using the constitutive parameters obtained from the uniaxial test underestimates the reaction force of the prescribed displacement. Conversely, using the identified constitutive parameters the global response of the specimen is captured accurately under prescribed displacement as well as under prescribed forces. This difference is explained by examining the stress/strain curves that are compared in Fig. 18. The uniaxial experiment gives lower stress level what influences the global response of the specimen when the constitutive parameters identified from this experiment are used. However, considering the scatter in the experimental data, it can be concluded that all the identified values are within the range of confidence.

#### 5.4. I-MIC3D with two cameras

The same behavior is obtained if the I-MIC3D method is applied to images from a stereo-vision system as illustrated in Fig. 19. Fig. 20 allows to compare the results for the two optical systems

using the finer mesh. The identified values are summarized in Table 1. It is confirmed that both identifications lead to constitutive parameters that are in very good agreement. The resulting stress/strain curves are compared to the result of a uniaxial experiment in Fig. 18. Fig. 21 allows to compare the von-Mises stress and equivalent accumulated plastic strain for I-MIC3D analysis with Mesh 1 and both the mono and stereo camera system. The field are similar which confirms the consistency of these analysis and the robustness of the proposed identification strategy.

#### 5.5. Correlation error analysis

In Fig. 22, the results are analyzed in terms of correlation error. First, we plot in Fig. 22(a) the evolution of the overall mean correlation error during the iterations for the identification of  $E$ ,  $S_y$  and  $H$  for the single camera system. For all the three stages of the analysis, a significant decrease of the correlation error is obtained. However, the optimization of the value of the Young modulus allows for a lower improvement. Fig. 22(b) shows the evolution of the mean correlation error after identification of the constitutive parameters. It is observed that for images of stage 0, the correlation error for I-MIC3D is close to the correlation for a pure DIC analysis what explain the lower reduction during the identification process. Conversely, for  $H$  and images of stage 2, a strong reduction of the error is obtained, up to 60% of its initial value. However, the correlation of I-MIC3D is slightly higher than the error for DIC. This was also observed in the previous section. In Fig. 22, it is also confirmed that the proposed I-MIC3D approach has a low sensitivity of the mesh size as the evolution of the mean correlation error for two mesh refinements is similar.

In Fig. 22 we also plot the evolution of the mean correlation error for the I-MIC3D analysis for a linear hardening law (only  $S_y$  and  $H$  are to be identified). We see that from the beginning of plasticity (mean strain from 0.005) to mean strain up to 0.04, a linear hardening law leads to significantly higher correlation error than the hardening law with a linear and a power law dependency. For larger mean strain, plasticity is fully developed with accumulated plastic strain level higher than 20% for which both models agree well in terms of stress/strain curve. However, when considering Fig. 23, the conclusion might be slightly different. Indeed, global responses are plotted in Fig. 23 and we can see that the response using the linear hardening law only deviates from the experimental response for mean strains from 0.005 to 0.01. Therefore, the correlation error al-

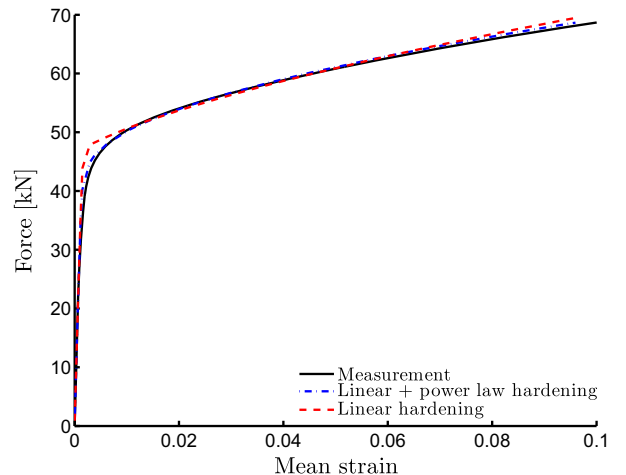


**Fig. 23.** Comparison of the load v.s. mean strain curves: experimental data and identification results for a linear and power law hardening and a linear hardening only.

lows for a more discriminating criterion to state if a constitutive law allows a more reliable description of the material behavior.

## 6. Conclusion

Identification and model validation were originally performed using global response of samples or structures. Nowadays, the development of full field measurement techniques such as DIC offers the opportunity to take benefit of a huge amount of data. This implies the need for the development of a dedicated strategy that can exploit efficiently the capabilities of full field measurement techniques. Existing strategies that can handle full field data to estimate constitutive model parameters are limited to two-dimensional mechanical models. In some cases such as finite strain plasticity, two-dimensional modeling is not acceptable and three-dimensional effects must be taken into account.

In this paper, we have introduced an identification strategy that mixes intimately numerical simulations with DIC, and that can overcome the common limitations of existing identification methods. In the proposed framework, one, two or more cameras can be used. The mechanical model is 3D and finite strains are considered. Being an extension of optimal techniques in terms of noise robustness proposed in Réthoré (2010) or Leclerc et al. (2009), the proposed approach has the same robustness. Based on a virtual testing procedure, the performances of the proposed method were evaluated. We showed that a low sensitivity to initial parameter guess and to mesh refinement is obtained. Then a real experiment was analyzed. Again the robustness of the proposed approach could be underlined. Further, it is possible to discriminate between two constitutive models that give similar global responses. The use of such a technique is promising not only for the identification of constitutive model parameters but also e.g., for fracture or yielding criteria in a general context.

## References

- Avril, S., Bonnet, M., Bretelle, A., Grediac, M., Hild, F., Jeny, P., Latourte, F., Lemosse, D., Pagano, S., Pagnacco, E., et al., 2008. Overview of identification methods of mechanical parameters based on full-field measurements. *Experimental Mechanics* 48 (4), 381–402.
- Besnard, G., Hild, F., Roux, S., 2006. 'finite-element' displacement fields analysis from digital images: application to portevin-le châtelier bands. *Experimental Mechanics* 46 (6), 789–803.
- Bui, H., Constantinescu, A., Maigre, H., 2004. Numerical identification of linear cracks in 2d elastodynamics using the instantaneous reciprocity gap. *Inverse Problems* 20, 993.
- Claire, D., Hild, F., Roux, S., 2004. A finite element formulation to identify damage fields: the equilibrium gap method. *International Journal for Numerical Methods in Engineering* 61, 189–208.
- Grédiac, M., 1989. Principe des travaux virtuels et identification. *Comptes rendus de l'Académie des sciences. Série 2, Mécanique, Physique, Chimie, Sciences de l'univers, Sciences de la Terre* 309 (1), 1–5.
- Grédiac, M., Pierron, F., Avril, S., Toussaint, E., 2006. The virtual fields method for extracting constitutive parameters from full-field measurements: a review. *Strain* 42 (4), 233–253.
- Kavanagh, K., Clough, R., 1971. Finite element applications in the characterization of elastic solids. *International Journal of Solids and Structures* 7, 11–23.
- Leclerc, H., Perie, J., Roux, S., Hild, F., 2009. *Computer Vision/Computer Graphics Collaboration Techniques*. Springer, Berlin (Chapter. Integrated Digital Image Correlation for the Identification of Mechanical Properties).
- Lecompte, D., Smits, A., Sol, H., Vantomme, J., Van Hemelrijck, D., 2007. Mixed numerical-experimental technique for orthotropic parameter identification using biaxial tensile tests on cruciform specimens. *International Journal of Solids and Structures* 44 (5), 1643–1656.
- Pagnacco, E., Moreau, A., Lemosse, D., 2007. Inverse strategies for the identification of elastic and viscoelastic material parameters using full-field measurements. *Materials Science and Engineering: A* 452–453, 737–745.
- Réthoré, J., 2010. A fully integrated noise robust strategy for the identification of constitutive laws from digital images. *International Journal for Numerical Methods in Engineering* 84, 631–660.
- Réthoré, J., Hild, F., Roux, S., 2009. An extended and integrated digital image correlation technique applied to the analysis of fractured samples. *European Journal of Computational Mechanics* 18, 285–306.
- Rossi, M., Pierron, F., 2011. Identification of plastic constitutive parameters at large deformations from three dimensional displacement fields. *Computational Mechanics*, 1–19.
- Sun, Y., Pang, J., Wong, C., Su, F., 2005. Finite-element formulation for a digital image correlation method. *Applied Optics* 44 (34), 7357–7363.
- Sutton, M., Wolters, W., Peters, W., Ranson, W., McNeill, S., 1983. Determination of displacements using an improved digital correlation method. *Image Vision Computing* 1 (3), 133–139.
- Wu, T., Coret, M., Combescure, A., 2011. Strain localisation and damage measurement by full 3d digital image correlation: Application to 15–5ph stainless steel. *Strain* 47 (1), 49–61.